Optics Letters

Optimization-based simultaneous alignment and reconstruction in multi-element tomography

Zichao (Wendy) Di,[1,2,*] Si Chen,[2] Doga Gursoy,[2,3] Tatjana Paunesku,[4] Sven Leyffer,[1] Stefan M. Wild,[1] and Stefan Vogt[2]

[1]Mathematics and Computer Science Division, Argonne National Laboratory, 9700 South Cass Avenue, Lemont, Illinois 60439, USA
[2]X-ray Science Division, Argonne National Laboratory, 9700 South Cass Avenue, Lemont, Illinois 60439, USA
[3]Department of Electrical and Computer Engineering, Northwestern University, 2145 Sheridan Road, Evanston, Illinois 60208, USA
[4]Department of Radiation Oncology, Northwestern University, 303 East Chicago Avenue, Chicago, Illinois 60611, USA
*Corresponding author: wendydi@anl.gov

Received 17 July 2019; accepted 27 July 2019; posted 1 August 2019 (Doc. ID 372850); published 26 August 2019

As x-ray microscopy is pushed into the nanoscale with the advent of more bright and coherent x-ray sources, associated improvement in spatial resolution becomes highly vulnerable to geometrical errors and uncertainties during data collection. We address a form of error in tomography experiments, namely, the drift between projections during the tomographic scan. Our proposed method can simultaneously recover the drift, while tomographically reconstructing the specimen based on a joint iterative optimization scheme. This approach utilizes the correlation provided from different view angles and different signals. While generally applicable, we demonstrate our method on x-ray fluorescence tomography from a tissue specimen and compare the reconstruction quality with conventional methods.

https://doi.org/10.1364/OL.44.004331

X-ray fluorescence (XRF) microscopy enables the visualization of elemental content in applications from scientific areas as diverse as materials science, life sciences, and environmental science [1]. By collecting the fluorescence signal from different view angles of the sample (namely, the sinogram), one can carry out a three-dimensional (3D) reconstruction of elemental composition in the sample [2–6]. To acquire high spatial resolution datasets with minimum radiation damage, one usually employs scanning-probe-based imaging, where a small x-ray beam is raster-scanned across the sample, and the fluorescence signal is collected by an energy-dispersive detector [7–9]. With recent advances in the development of x-ray optics, elemental mapping can now reach a spatial resolution below 10 nm in two dimensions (2D) [10]. In order to maintain this spatial resolution in 3D; however, an accurate alignment of projections around the common rotation axis is required. In other words, an improved 3D spatial resolution is highly susceptible to geometrical errors during the scan, in particular, the horizontal drifts (e.g., center-of-rotation, sample, and beam drifts), which are the major causes of misalignment in the projections. Figure 1 illustrates a standard experimental setup for tomographic imaging. The lack of measurement error calibration will lead to smeared images with decreased spatial resolution and reduced contrast; in the worst case, this can result in misinterpretation of the imaged structure.

In the case of negligible drifts compared with the image resolution, it is sufficient to reconstruct the uncalibrated projections by using iterative procedures (e.g., maximum likelihood) with regularizations to enforce prior knowledge such as sparsity or smoothness [11–13]. However, these approaches do not address nontrivial drift (e.g., dynamic sample drifts on the order of pixel resolution during the course of experiments). The common practice of error calibration is performed separately before the reconstruction step by area- or feature-based image registration of consecutive projections (e.g., cross-correlation). An alternative is to use a distinguishable feature such as a hotspot in the sample or a fiducial marker, and track it through the projections. This approach, however, is sometimes invasive and requires a significant amount of expert input [14–17]. Even if the projections are perfectly aligned, an extra step of finding the center of rotation is required. An example of an automated approach is the class of iterative methods that use the consistency of the solutions of the forward and inverse problems by alternating the reconstruction and alignment steps until the simulated projections match the measurements [18–23]. One common feature of these iterative methods is the search for the alignment parameters; these methods can yield better accuracy in terms of noise and angular requirements, but still can fall short for the cases when the drift is significant.

X-ray fluorescence tomography yields multiple elemental signals simultaneously with an energy-resolving detector and, thus, all elemental signals have the same experimental error. A practical approach then is to align an elemental channel with good signal-to-noise ratio (SNR), and then apply the recovered shifts to other individual elemental channels. However, because the reconstruction of the object is not used as part of the drift correction, this approach can fail for cases with poor SNR. Therefore, instead of performing alignment on a single channel with a high SNR, it is desirable to learn correlations among different elemental channels and exploit their complementary

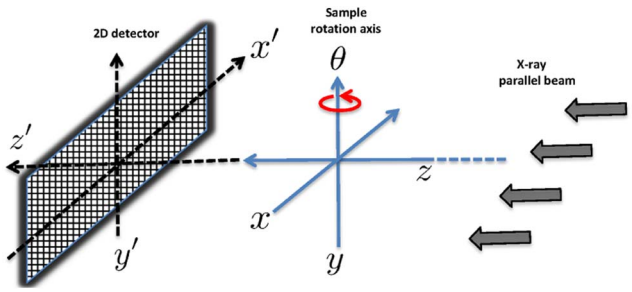

Fig. 1. Experiment geometry of 3D tomography. In this Letter, we address horizontal drifts, which are primarily caused by center-of-rotation, sample, and beam drifts.

information in order to robustly recover the misalignment and drop the dependency on a single "good" channel.

We report on a flexible and robust inversion framework that performs simultaneous alignment and reconstruction of the multiple elemental channels. The proposed framework exploits the fact that an optimal reconstruction can be achieved only when the projections are properly aligned, and the natural complementary information embedded in multiple channels is used to overcome the ill-conditioned (i.e., limited-angle) nature of challenging tomography problems. One feature of the proposed method common to other iterative approaches is that it assumes that the center of rotation aligns with the center of the detector's field of view. This feature greatly distinguishes an iterative approach from the manual approach, since it avoids the extra step of finding the shared center of rotation among projections.

We use θ and τ to index, respectively, the x-ray beam angle and beamlet from a collection of N_θ angles and N_τ beamlets; v indexes a set of N_v spatial voxels used to discretize the sample. We denote the intersection lengths (in centimeters) of beamlet (θ, τ) with the voxel v by $\mathbf{L} \in \mathbb{R}^{N_\theta N_\tau \times N_v}$; it corresponds to the discrete Radon transform operator for a (drift-free) experimental configuration. We use e to index N_e possible chemical elements. The goal of x-ray fluorescence tomography is to recover $\mathcal{W} \in \mathbb{R}^{N_v N_e}$, the concentration (in $\mathrm{g\,cm^{-3}}$) of element e in voxel v.

One way to address the misalignment is to explicitly recover the experimental configuration (e.g., sample and scanning position), which can be embedded in the forward Radon transform operator. However, this is computationally expensive given the iterative construction of $\mathbf{L}$ with the dependency on the unknown experiment parameters. Instead, we utilize the numerical approach in [24], which seeks the optimal shifting parameters to translate the misaligned projection (i.e., with drift error) to drift-free projection in order to optimally match the nominal $\mathbf{L}$.

Let $\mathbf{D}^e = [\mathbf{D}^e_\theta] \in \mathbb{R}^{N_\theta \times N_\tau}$ be the misaligned (i.e., observed) sinogram of the eth element and its projection at angle θ be $\mathbf{D}^e_\theta \in \mathbb{R}^{N_\tau}$. We let $\acute{\mathbf{D}}^e = [\acute{\mathbf{D}}^e_\theta]$ be the drift-free sinogram. Given the sifting property [25], there exists $P_\theta \in \mathbb{R}$ so that

$$\acute{\mathbf{D}}^e = [\mathbf{D}^e_\theta * \delta(\boldsymbol{\tau} - P_\theta)], \tag{1}$$

where δ is the Dirac delta, and $*$ denotes convolution. The singularity of δ poses challenges for numerical methods; therefore, we introduce an approximation of Eq. (1):

$$\acute{\mathbf{D}}^e \approx g(\mathbf{D}^e, \mathbf{P}) = \left[\mathbf{D}_\theta * \left(\frac{1}{\sigma\sqrt{2\pi}} \exp\left\{\frac{-(\boldsymbol{\tau} - P_\theta)^2}{2\sigma^2}\right\}\right)\right], \tag{2}$$

where the delta function δ is approximated by a Gaussian function. We choose $\sigma = 1/2.355 \approx 0.42$, where the full-width at half-maximum (FWHM) of the Gaussian is one unit of the beam width (2.355 is the FWHM of the standard Gaussian), so that smoothing artifacts introduced by the Gaussian approximation used in Eq. (2) are smaller than the actual beam width.

Denoting $\mathbf{P} = [P_\theta]_{\theta=1}^{N_\theta} \in \mathbb{R}^{N_\theta}$, our goal is to recover $\mathcal{W}$ and $\mathbf{P}$ simultaneously. Given that the XRF data is derived from measured photon counts, we can formulate a loss function for each element by following a maximum likelihood approach that assumes the measurements are subject to independent Poisson noise [26,27] for each e:

$$\begin{aligned} &\min_{\mathcal{W}(:,e)\geq 0, \mathbf{P}} \quad \phi^e(\mathcal{W}(:,e), \mathbf{P}) \\ &\quad = \mathbf{1}^T(\mathbf{L}\mathcal{W}(:,e) - \ln(\mathbf{L}\mathcal{W}(:,e))\mathrm{vec}(g(\mathbf{D}^e, \mathbf{P}))), \end{aligned} \tag{3}$$

where $\mathbf{1} \in \mathbb{R}^{N_\theta N_\tau}$ is a vector of ones, and $\mathrm{vec}(\cdot)$ denotes the vectorized matrix. Here we instead propose a joint inversion coupling multiple elemental channels, which results in the optimization problem

$$\min_{\mathcal{W}\geq 0, \mathbf{P}} \phi(\mathcal{W}, \mathbf{P}) = \frac{1}{2}\sum_{e=1}^{N_e} \alpha_e \phi^e(\mathcal{W}(:,e), \mathbf{P}), \tag{4}$$

where $\alpha_e > 0$ balances the relative ability and variability of each elemental channel to fit the data. Note that one also can use multiple energy channels instead of the elemental channels to avoid possible elemental decomposition artifacts [13]. Given $s(\mathbf{D}^e)$ as the standard deviation of data $\mathbf{D}^e$, we choose, $\alpha_e = s(\mathbf{D}^e)/\sum_{e=1}^{N_e} s(\mathbf{D}^e)$. An alternative choice is based on the peak intensity of the signal to determine the relative contribution from each channel. Overall, the contribution of each elemental channel to the final inversion should be proportional to its SNR.

Since the approximation in Eq. (2) admits an analytic calculation of $\partial\phi^e/\partial\mathbf{P}$ and $\partial\phi^e/\partial\mathcal{W}$, we employ a derivative-based algorithm, the truncated Newton method [28], to minimize the problem in Eq. (4). The nonnegative constraint is enforced by the projected conjugate gradient method [29].

We illustrate the performance of the proposed joint inversion on experimental data. For demonstration purposes, we reconstruct only a 2D cross section of the 3D dataset. A micrometer-thick human neuroblastoma cell line SK-N-DZ (ATCC Catalog No. CRL-2149), grown according to manufacturer's suggestions as a monolayer on a silica nitride window, was imaged under cryogenic conditions at beamline 9-ID-B at the Advanced Photon Source by using the Bionanoprobe [30]. Fluorescence tomographic data were sampled on a subregion of the sample by collecting 48 projections over 141° sample rotation. Each projection was 8.2 μm × 13 μm with a 100 nm pixel size, acquired by scanning the sample across a 10 keV focused x-ray beam. A full spectrum was acquired for each pixel. The 2D elemental maps (sinogram of each element) were decomposed from the full spectra and generated using MAPS [31]; see the top row of Fig. 2. Due to instrumentation limitations such as rotation stage radial runout and flatness, there is misalignment between projections, which needs to be corrected before a meaningful reconstruction. The existence of horizontal drifts is evidenced by the jitter (especially clear in the Ti sinogram). We seek to recover six elements (P, S, Ca, Ti, Fe, and Zn) via tomography reconstruction on the decomposed 2D elemental maps.

We compare the proposed joint inversion (labeled as "joint") with two representative types of current practices: the manual

and alternating approaches. The alternating approach represents a class of "iterative reprojection" techniques, which finds **P** for a given sinogram by alternating between iterative alignment steps and tomographic reconstruction steps. We use the alternating approach reported in [20] due to its superior performance compared with other existing approaches and its availability in TomoPy v1.2.1 [32], a popular Python package for tomographic data processing and image reconstruction. Notice that cross-correlation is used for registration of reprojected and measured data in the alternating approach. The manual approach is based on manually tracking a hotspot, which is an isolated/distinguishable feature. Because of its high contrast and simplicity, here we use the titanium (Ti) channel sinogram. We use the peak signal in each projection as the hotspot, manually align this identified spot in all the projections to the first projection's hotspot, extract the required shifts for each projection, and apply these shifts to all the other elemental channels. Notice that these shifts can only align the projections to the same center of rotation; we still need to find this common center of rotation to perform the reconstruction. In the case of Ti, it is simply the peak signal location. To further demonstrate the robustness of the proposed joint inversion, we show its three variants with different sets of elemental channels: (1) joint inversion dropping the dependency on the "good" channel (Ti); (2) single elemental inversion by solving problem (3) separately for each element; and (3) joint inversion dropping the "bad" channels (P and S).

In Fig. 2, we show the alignment results of the original data comparing the six different approaches: alternate (second row), manual (third row), joint-no-Ti (fourth row), separate (fifth row), joint-no-PS (sixth row), and joint (seventh row). We also show their corresponding reconstructions in the last row. We

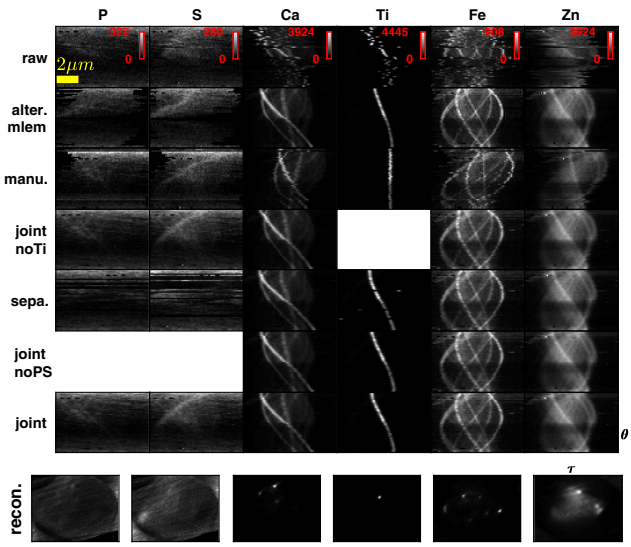

Fig. 2. Alignment of elemental sinograms with their reconstructions. Top row, raw sinogram without alignment; second row, aligned sinogram via alternate approach; third row, manual alignment via hotspot reference; fourth row, aligned sinogram via proposed joint inversion without a Ti channel; fifth row, separate alignment of each element by solving proposed framework Eq. (3); sixth row, aligned sinogram via proposed joint inversion without P and S channels; seventh row, aligned sinogram via proposed joint inversion with all available channels. All the approaches return comparable results in terms of aligning Ca, Ti, Fe, and Zn channels while, comparable with manual alignment, automated inversion is more automatic and robust. The last row shows the corresponding elemental reconstructions.

fix the initial guesses to all tests as 0s, and the optimization stops when it satisfies the criteria $\|\nabla\phi\| \leq 1e-6$. The results are comparable in terms of aligning Ca, Ti, Fe, and Zn by eliminating jitter, but not the P and S signals due to their relatively uniform and low contrast.

We can further extract the shifts (i.e., **P**) returned by various approaches used to align the sinograms. Since the manual and automated approaches assume different centers of rotation where iterative approaches always assume that the center of rotation aligns with the center of detector's field of view, we only compare the results from the automated methods (i.e., alternate, separate, joint-no-Ti, joint-no-PS, and joint). Notice that for joint-type approaches, only one set of shifts is returned regardless of the number of combined sinograms, while the separate and alternate approaches return a set of shifts for each sinogram. The result is reported in Fig. 3. Since the differences of each shift P_θ obtained by the five different approaches are small compared to the median, we choose the median as the "ground truth" of P_θ, and further test the sensitivity and robustness of each approach to a synthetically adjusted SNR ratio. Since XRF imaging follows Poisson statistics, we approximate its corresponding SNR as $\sqrt{n}$, where n is the total photon count of each elemental map. We focus on the elements Ca, Ti, Fe, and Zn.

We first reduce the SNR to 30%, 18%, 12%, 9%, 6%, and 3% of the SNR of the original sinograms by applying Poisson noise with the reduced SNR as the mean. We perform alternate, separate, and joint (combining the four available channels) and compare the difference between the recovered $P_\theta(\mathrm{SNR})$ (as a function of SNR) and the ground truth P_θ. Figure 4 shows the aligned sinograms with 18% of the original SNR. With relatively similar results for Ca, Ti, and Zn from the three different approaches, the joint aligns the Fe channel the best compared to the other two approaches. The overall performance comparison in Fig. 5 shows the variations of the error $P_\theta(\mathrm{SNR}) - P_\theta$ obtained by three different approaches for gradually reduced SNR. We see that it is harder to align data with lower SNRs. The spread of recovery accuracy by the joint approach remains small compared with the other two approaches, however, and this observation indicates that the joint is more robust to different levels of noise in the data.

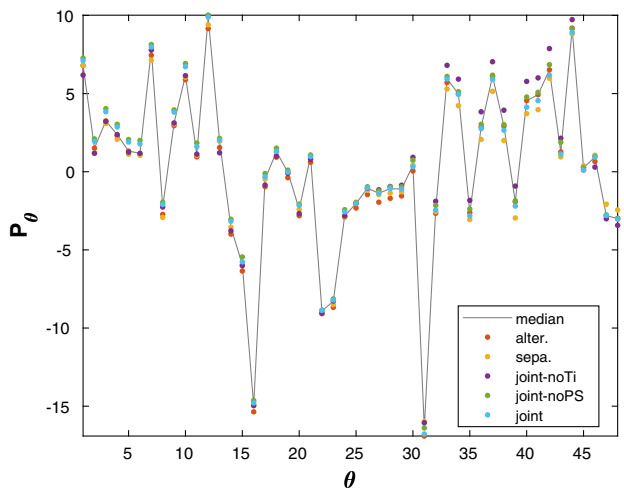

Fig. 3. Shift of each projection P_θ obtained by the five approaches (alternate, separate, joint-no-Ti, joint-no-PS, and joint) agrees well. This result indicates that the shifts recovered for the raw data are reliable and can be considered as ground truth.

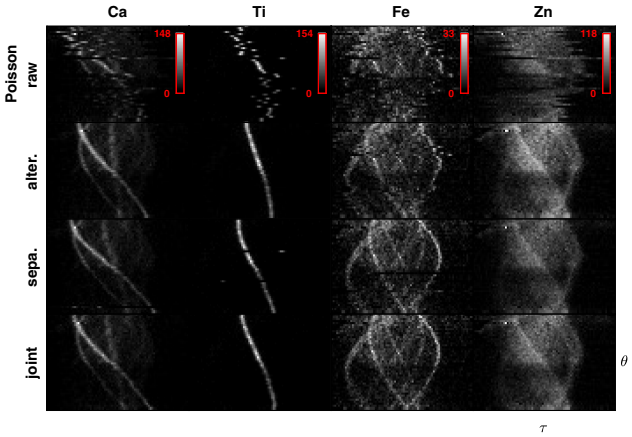

Fig. 4. Alignment of elemental sinograms with 18% of the original SNR. Top row, raw sinogram with reduced SNR; second row, aligned sinogram via alternate; third row, separate alignment of each element by solving Eq. (3); fourth row, aligned sinogram via proposed joint inversion with four channels. Joint inversion outperforms the other two approaches.

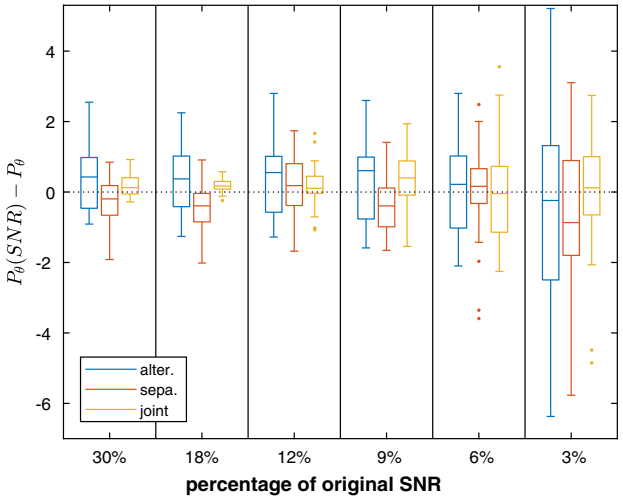

Fig. 5. Distribution of the P_θ(SNR) – P_θ errors (based on ground truth P_θ from 100% SNR) for synthetically reduced SNR levels. The boxes indicate 25%, 50%, and 75% quantiles. The joint approach shows better robustness and less sensitivity against noise, compared to the other two approaches.

We formulate an inverse problem to simultaneously calibrate the misalignment and reconstruct the elemental composition under an x-ray fluorescence tomography paradigm. The proposed model provides a flexible reconstruction framework to combine multiple signals and exploits the correlation and complementary information provided by multiple elemental channels, given that they are captured from the same sample under the same experimental setup; the model provides a robust and automatic reconstruction that outperforms the current practice on an experimental dataset. Novel approaches such as this are vital to realizing the full 3D resolution offered by the latest x-ray optics and source developments. The extension of the proposed algorithm to 3D reconstruction is natural. A future direction is to explore computing strategies to accelerate the overall processing time (not just by parallelizing 3D slices, but by carrying out in-plane parallelization).

Funding. Office of Science (DE-AC02-06CH11357).

Acknowledgment. The authors thank Francesco De Carlo for helpful discussions.

REFERENCES

1. T. Paunesku, S. Vogt, J. Maser, B. Lai, and G. Woloschak, J. Cell. Biochem. **99**, 1489 (2006).
2. J. P. Hogan, R. A. Gonsalves, and A. S. Krieger, IEEE Trans. Nucl. Sci. **38**, 1721 (1991).
3. E. X. Miqueles and A. R. De Pierro, IEEE Trans. Med. Imaging **30**, 438 (2011).
4. C. Gramaccioni, Y. Yang, A. Procopio, A. Pacureanu, S. Bohic, E. Malucelli, S. Iotti, G. Farruggia, I. Bukreeva, A. Notargiacomo, M. Fratini, P. Valenti, L. Rosa, F. Berlutti, P. Cloetens, and S. Lagomarsino, Appl. Phys. Lett. **112**, 053701 (2018).
5. B. Golosio, A. Somogyi, A. Simionovici, P. Bleuet, J. Susini, and L. Lemelle, Appl. Phys. Lett. **84**, 2199 (2004).
6. C. G. Schroer, Appl. Phys. Lett. **79**, 1912 (2001).
7. P. Horowitz and J. A. Howell, Science **178**, 608 (1972).
8. C. Ryan, R. Kirkham, R. Hough, G. Moorhead, D. Siddons, M. De Jonge, D. Paterson, G. De Geronimo, D. Howard, and J. Cleverley, Nucl. Instrum. Methods Phys. Res. A **619**, 37 (2010).
9. Y. Sun, S.-C. Gleber, C. Jacobsen, J. Kirz, and S. Vogt, Ultramicroscopy **152**, 44 (2015).
10. H. Yan, N. Bouet, J. Zhou, X. Huang, E. Nazaretski, W. Xu, A. P. Cocco, W. K. Chiu, K. S. Brinkman, and Y. S. Chu, Nano Futur. **2**, 011001 (2018).
11. K. Niinimaki, M. Lassas, K. Hamalainen, A. Kallonen, V. Kolehmainen, E. Niemi, and S. Siltanen, SIAM J. Imaging Sci. **9**, 938 (2016).
12. F. Mahmood, N. Shahid, U. Skoglund, and P. Vandergheynst, IEEE Signal Process. Lett. **25**, 700 (2018).
13. D. Gürsoy, T. Bicer, A. Lanzirotti, M. G. Newville, and F. D. Carlo, Opt. Express **23**, 9014 (2015).
14. D. E. Olins, A. L. Olins, H. A. Levy, R. C. Durfee, S. M. Margle, E. P. Tinnel, and S. D. Dover, Science **220**, 498 (1983).
15. J. Lim, H. Kim, and S. Y. Park, J. Synchrotron Radiat. **21**, 827 (2014).
16. M. Cao, A. Takaoka, H.-B. Zhang, and R. Nishi, J. Electron Microsc. **60**, 39 (2010).
17. R. Han, L. Wang, Z. Liu, F. Sun, and F. Zhang, J. Struct. Biol. **192**, 403 (2015).
18. S. Tomonaga, M. Baba, and N. Baba, Microscopy **63**, 279 (2014).
19. M. Storm, F. Beckmann, and C. Rau, Opt. Lett. **42**, 4982 (2017).
20. D. Gürsoy, Y. P. Hong, K. He, K. Hujsak, S. Yoo, S. Chen, Y. Li, M. Ge, L. M. Miller, Y. S. Chu, V. De Andrade, K. He, O. Cossairt, A. K. Katsaggelos, and C. Jacobsen, Sci. Rep. **7**, 11818 (2017).
21. T. Ramos, J. S. Jørgensen, and J. W. Andreasen, J. Opt. Soc. Am. A **34**, 1830 (2017).
22. H. Yu, S. Xia, C. Wei, Y. Mao, D. Larsson, X. Xiao, P. Pianetta, Y.-S. Yu, and Y. Liu, J. Synchrotron Radiat. **25**, 1819 (2018).
23. M. Guizar-Sicairos, J. J. Boon, K. Mader, A. Diaz, A. Menzel, and O. Bunk, Optica **2**, 259 (2015).
24. A. Austin, Z. W. Di, S. Leyffer, and S. M. Wild, SIAM J. Sci. Comput. **41**, B497 (2019).
25. R. N. Bracewell and R. N. Bracewell, *The Fourier Transform and Its Applications* (McGraw-Hill, 1986), Vol. **31999**.
26. T. J. Holmes and Y.-H. Liu, J. Opt. Soc. Am. A **8**, 893 (1991).
27. J. A. Browne and T. J. Holmes, Appl. Opt. **33**, 3010 (1994).
28. S. G. Nash, J. Comput. Appl. Math. **124**, 45 (2000).
29. J. Nocedal and S. J. Wright, *Numerical Optimization* (Springer, 2006).
30. S. Chen, T. Paunesku, Y. Yuan, J. Deng, Q. Jin, Y. Hong, D. Vine, B. Lai, C. Flachenecker, B. Hornberger, K. Brister, C. Jacobsen, G. E. Woloschak, and S. Vogt, AIP Conf. Proc. **1696**, 020028 (2016).
31. S. Vogt, J. Phys. IV **104**, 635 (2003).
32. D. Gürsoy, F. De Carlo, X. Xiao, and C. Jacobsen, J. Synchrotron Radiat. **21**, 1188 (2014).